

LOW-FREQUENCY MODAL AND NON-MODAL STABILITY OF A TURBULENT SEPARATION BUBBLE

Carolina Cura

Institute of Aeronautics and Astronautics
Technische Universität Berlin
10587 Berlin, Germany
c.cura@tu-berlin.de

Ardeshir Hanifi

FLOW, Engineering Mechanics
KTH Royal Institute of Technology
100 44 Stockholm, Sweden
hanifi@kth.se

André V. G. Cavalieri

Divisão de Engenharia Aeronáutica
Instituto Tecnológico de Aeronáutica
12228-900 São José dos Campos, Brazil
andre.cavalieri@gp.ita.br

Julien Weiss

Institute of Aeronautics and Astronautics
Technische Universität Berlin
10587 Berlin, Germany
julien.weiss@tu-berlin.de

1 ABSTRACT

The low-frequency receptivity of an incompressible, pressure-gradient-induced turbulent separation bubble (TSB) is investigated with the aim of studying the mechanism responsible for the low-frequency unsteadiness commonly observed in experimental studies. The investigated flow consists of a TSB generated on a flat plate by means of adverse and favorable pressure gradients. The direct numerical simulation of Coleman *et al.* (2018) is used for the linear analysis and compared to the unsteady flow database of Le Floc’h *et al.* (2018, 2020). Resolvent analysis (RA) reveals receptivity to external forcing at low frequency and low, non-zero spanwise wavenumber. This low-frequency receptivity can be related to the experimentally observed low-frequency “breathing” of the bubble through the alignment metric, which exceeds 94%. Finally, the strong similarities between the least stable mode of the global linear stability analysis and the optimal response of RA suggests that the low-frequency breathing motion might be caused by a modal mechanism, driven by this weakly damped global mode.

2 INTRODUCTION

Turbulent separation bubbles (TSBs) arise when a turbulent boundary layer separates from a solid surface and subsequently reattaches downstream of the separation line. TSBs are known to exhibit unsteadiness along various spatial and temporal scales, thereby diminishing the performance of the system under consideration. Such detrimental effects may include reduced lift, increased drag, noise emission or vibrations. Hence, the understanding of these unsteady phenomena holds particular significance within the fluid dynamics community. When considering pressure-induced turbulent separation bubbles (Na & Moin, 1998), generally, three distinct frequency ranges are distinguished by means of the Strouhal number $St = fL_b/U_{ref}$ based on the separation length L_b and the reference velocity U_{ref} . At relatively high Strouhal number $St > 1$, high-frequency fluctuations are caused by small-scale turbulent motions (Abe, 2017). Further, the roll-up and shedding of vortices from the shear layer bounding the recirculation

region has been associated with a characteristic Strouhal number $St \simeq 0.1 - 1$ (Kiya & Sasaki, 1983; Cherry *et al.*, 1984). Finally, a low-frequency unsteadiness related to the temporal expansion and contraction of the entire separation bubble has been observed at $St \simeq 0.01 - 0.1$ (Mohammed-Taifour & Weiss, 2016). This low-frequency unsteadiness (“breathing”) of the TSB, is the main focus of the present work. While the low-frequency unsteadiness of pressure-induced TSBs has been extensively documented for high-speed flow configurations, e.g., featuring shockwave/boundary layer interactions (SBLI) (Dolling, 2001), research on the low-frequency unsteadiness of pressure-induced TSBs in the subsonic regime has only recently emerged (e.g., Mohammed-Taifour & Weiss, 2016; Wu *et al.*, 2020; Richardson *et al.*, 2023).

If the proposed mechanisms for the emergence of low-frequency unsteadiness in turbulent SBLIs equally apply to subsonic TSBs, two main categories can be distinguished (Clemens & Narayanaswamy, 2014). The first entails an upstream mechanism, where velocity fluctuations within the incoming boundary layer directly influence the position and size of the TSB. Here, the low-frequency unsteadiness is attributed to the presence of large-scale “superstructures” observed in both subsonic and supersonic turbulent boundary layers. The second category, a downstream mechanism, implicates the existence of inherent flow instabilities within the TSB. Both shear layer and centrifugal instabilities have been considered (Wu *et al.*, 2020).

In this work, we examine a TSB generated on a flat test surface by a combination of adverse and favourable pressure gradients. This flow configuration has been previously studied experimentally by Le Floc’h *et al.* (2018, 2020) and numerically via DNS by Coleman *et al.* (2018). Our procedure is as follows: we perform linear stability analysis on a base flow consisting of the average DNS flow field and we cross-validate our results with the unsteady experimental database.

3 NUMERICAL DATABASE

In this work, we investigate the low-frequency receptivity of the time- and spanwise-averaged velocity field extracted

from the DNS by Coleman *et al.* (2018). The flow field features a fully turbulent, two-dimensional flat-plate boundary layer subjected to an APG followed by a FPG. The APG-FPG characteristics are imposed by a transpiration velocity profile $V_{\text{top}}(x)$ (Eq. 1) on a virtual parallel plane at a fixed distance opposite to the no-slip wall, where V_{max} represents the maximum velocity of the transpiration velocity profile and ξ denotes the length scale. To suppress boundary-layer separation on the wall, a constant boundary-layer bleed velocity Φ_{top} is introduced.

$$V_{\text{top}}(x) = -\sqrt{2}V_{\text{max}}\left(\frac{x}{\xi}\right)\exp\left(\frac{1}{2} - \left(\frac{x}{\xi}\right)^2\right) + \phi_{\text{top}} \quad (1)$$

The solution to the incompressible Navier-Stokes equations was computed using a pseudo-spectral code. Further details about the DNS are available in Coleman *et al.* (2018). Only the mean flow field from case C (main case) will be considered hereafter.

Traditionally, stability analyses employing DNS base flows are compared to unsteady DNS data. However, we opt to compare our results with the experimental database of Le Floc’h *et al.* (2018, 2020) for two main reasons. Firstly, Coleman *et al.* (2018) did not observe a low-frequency breathing motion in their DNS due to computational limitations (their sampling period was $66L_b/U_{\text{ref}}$ while breathing occurs at $0.01U_{\text{ref}}/L_b$). Secondly, if our linear analysis aligns with experimental findings, it would strongly support the generality and portability of our results, while simultaneously ruling out the presence of experimental artifacts. Consequently, even though the DNS of Coleman *et al.* (2018) was not originally designed to match our experimental TSB flow, we argue that the benefits of our approach outweigh its drawbacks.

4 EXPERIMENTAL DATABASE

The experiments of Le Floc’h *et al.* (2018, 2020) were performed in the TFT boundary-layer wind tunnel, a blow-down type tunnel specifically designed for the investigation of low-speed turbulent separation bubbles (Mohammed-Taifour & Weiss, 2016). The widening and subsequent converging wind tunnel floor is used to generate a combination of adverse and favorable pressure gradients, leading to mean flow separation (and reattachment) on the upper surface of the tunnel. A boundary-layer bleed on the lower surface of the tunnel is used to ensure that the boundary layer remains attached on the wind tunnel floor. The wind tunnel features a test section measuring 3 m in length and 0.6 m in width. The experiments were performed at a reference velocity $U_{\text{ref}} = 25 \text{ m s}^{-1}$, with a

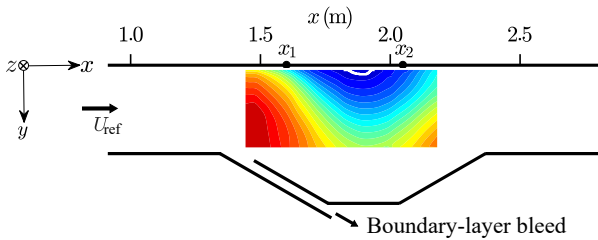


Figure 1. Schematic of wind tunnel test section, depicting the mean streamwise velocity field on the centerline. The time-averaged position of the TSB is indicated by the dividing streamline (white solid line). The positions of unsteady wall-pressure measurements are x_1, x_2 .

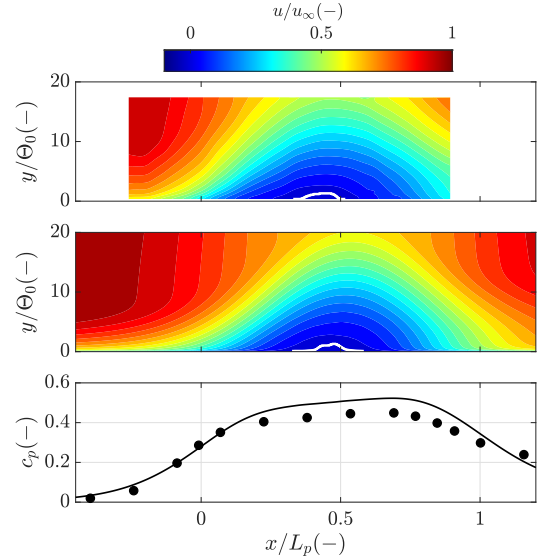


Figure 2. Streamwise velocity component u/u_{∞} of experimental flow field (top) and DNS flow (center). The time-averaged position of the TSB is indicated by the dividing streamline (white solid line). The pressure distribution along the flat plate is displayed by means of the pressure coefficient c_p (bottom) for the DNS flow (solid line) and the experimental TSB flow (symbols).

Reynolds number of approximately 5000 based on the incoming ZPG boundary layer’s momentum thickness ($\Theta_{\text{in}} = 3 \text{ mm}$). In Le Floc’h *et al.* (2020) TSBs of different sizes were studied through the variation of the APG-FPG characteristics. Here, our primary focus is their medium TSB, which, as demonstrated in the following, is the closest to the DNS data provided by Coleman *et al.* (2018). The experimental dataset includes planar time-resolved Particle Image Velocimetry (TR-PIV) in the streamwise/wall-normal plane and unsteady wall-pressure measurements on the test section centerline ($z = 0 \text{ m}$) and over the wind-tunnel span. A schematic of the wind-tunnel test section, depicting the mean streamwise velocity field as well as the position of unsteady wall-pressure measurements, is displayed in figure 1. Further details regarding the experimental data can be obtained in the original publications of Mohammed-Taifour & Weiss (2016) and Le Floc’h *et al.* (2018, 2020). In figure 2, we demonstrate that the two TSB flows exhibit a high degree of similarity when a certain set of scaling parameters is selected. For this purpose, we introduce the parameter L_p , which is equal to the streamwise distance between the maximum APG and FPG. We further introduce the momentum thickness Θ_0 , which was computed by means of the von Kármán integral. It corresponds to the momentum thickness that would be reached at the streamwise position $x(V_{\text{top}} = 0)$ for a ZPG boundary layer (Coleman *et al.*, 2018). The streamwise velocity component of the experimental flow field from Le Floc’h *et al.* (2020) (top) and the DNS flow of Coleman *et al.* (2018) (center) is shown, respectively. For comparability, the experimental flow field has been inverted along the wall-normal axis. The pressure coefficient c_p along the flat plate (bottom) shows qualitative agreement over a large portion of the domain.

We now examine fluctuating wall-pressure data gathered in the spanwise direction by Le Floc’h *et al.* (2018). All pressure signals were obtained by using piezoresistive pressure transducers with a range of 1 psi (6.89 kPa) and an estimated

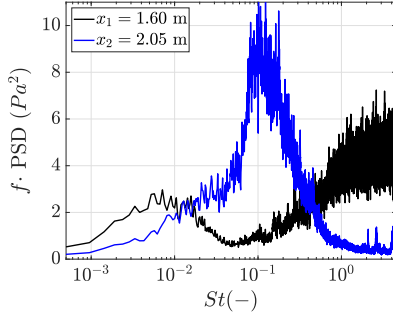


Figure 3. Pre-multiplied power spectral density (right) of unsteady wall-pressure measurements for two streamwise positions x_1, x_2 .

error of $\pm 5\%$. To eliminate low-frequency wind-tunnel noise in the signals, the correction method from Weiss *et al.* (2015) was applied. PSDs were calculated using Welch’s method with 50% overlap and a Hamming window.

Figure 3 presents the pre-multiplied Power Spectral Density (PSD) of the fluctuating wall pressure on the test-section centerline at two streamwise positions: one immediately upstream of the time-averaged location of the separation bubble ($x_1 = 1.60$ m) and another in the region downstream of the TSB ($x_2 = 2.05$ m), as depicted in figure 1. The low-frequency unsteadiness manifests as a distinct “hump” in the pre-multiplied PSD for $x_1 = 1.60$ m, where a significant amount of energy is concentrated in the region $St \simeq 0.01$. This low-frequency hump has been associated with the low-frequency breathing of the TSB in several works (e.g., Mohammed-Taifour & Weiss, 2016; Richardson *et al.*, 2023). Conversely, a different behavior is observed for $x_2 = 2.05$ m, where a peak is visible in the pre-multiplied PSD for $St \simeq 0.1$. Cura *et al.* (2023) linked this medium-frequency unsteadiness to convective instabilities in the shear layer bounding the recirculation region.

In figure 4 we show the two-point cross-correlation coefficient $R_{p'p'} = p'(z) * p'_{\text{ref}}(z_{\text{ref}}) / (p'_{\text{rms}} * p'_{\text{ref,rms}})$ at zero time lag measured by Le Floc’h *et al.* (2018) (symbols). The spanwise correlations were obtained by simultaneously measuring the fluctuating wall pressure at the test-section centerline ($z_{\text{ref}} = 0$ m) and with a moving sensor successively mounted at the spanwise positions $z = [0, \pm 0.05, \pm 0.10, \pm 0.15, \pm 0.20]$ m. All pressure signals were low-pass filtered with a cut-off frequency corresponding to $St = 0.03$. As indicated by figure 3, we focus on the low-frequency unsteadiness by examining the streamwise position $x_1 = 1.60$ m. A wave-like distribution of $R_{p'p'}$ across the span, characterized by a relatively large wavelength λ_z , becomes evident. This observation indicates that the low-frequency unsteadiness exhibits coherence across a significant portion of the test-section span. To quantify spanwise coherence, we proceed to perform a curve-fit of the correlation curve at $x_1 = 1.60$ m. We use the cosine function of the form $f(z) = c_1 \cdot \cos(c_2 z)$, and obtain the distribution displayed in figure 4 (solid line). Here, the fitted function has a non-dimensional spanwise wavenumber $\beta = 2\pi L_b / \lambda_z$ of 0.97. Notably, this value closely aligns with the spanwise wavenumber corresponding to the width of the wind tunnel $b = 0.6$ m, which is $\beta = 1.17$.

5 METHODS

In this section, we introduce the governing equations describing the TSB dynamics and briefly outline the stability

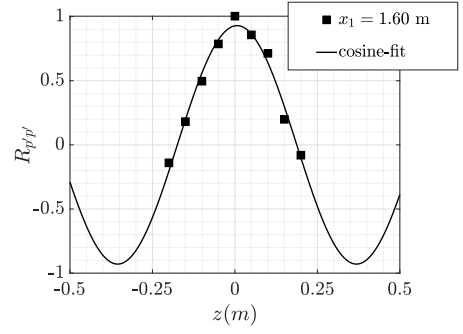


Figure 4. Spanwise correlation of low-pass filtered wall-pressure measurements (symbols) (modified from Le Floc’h *et al.*, 2020) and cosine-fit $f(z) = c_1 \cdot \cos(c_2 z)$ of pressure correlation at x_1 (solid line).

analysis methods employed in this work. Starting from the viscous incompressible Navier-Stokes equations, we decompose the flow field into time-averaged and fluctuating components according to $\mathbf{q}(x, y, z, t) = \bar{\mathbf{q}}(x, y, z) + \tilde{\mathbf{q}}(x, y, z, t)$. Introducing the above Reynolds decomposition into the incompressible Navier-Stokes equations and time-averaging leads to the linearized Navier-Stokes equations (LNSE)

$$\frac{\partial \tilde{\mathbf{u}}}{\partial t} + \tilde{\mathbf{u}} \cdot \nabla \bar{\mathbf{u}} + \bar{\mathbf{u}} \cdot \nabla \tilde{\mathbf{u}} = -\nabla \tilde{p} + \frac{1}{\text{Re}} (1 + \nu_t / \nu) \nabla^2 \tilde{\mathbf{u}} + \tilde{\mathbf{f}}_0, \quad (2)$$

$$\nabla \cdot \tilde{\mathbf{u}} = 0.$$

Here $\bar{\mathbf{u}} = (\bar{u}, \bar{v}, \bar{w})$ and $\tilde{\mathbf{u}} = (\tilde{u}, \tilde{v}, \tilde{w})$ are the streamwise, wall-normal and spanwise mean and fluctuating velocity, respectively, \tilde{p} is the fluctuating pressure, and Re is the Reynolds number. As proposed by McKeon & Sharma (2010), we group the non-linear terms in the Navier-Stokes equations into an unknown forcing term $\tilde{\mathbf{f}}_0$, and further, represent part of the Reynolds stresses by means of an eddy viscosity model (Reynolds & Hussain, 1972). The eddy viscosity is calculated from the DNS data (Coleman *et al.*, 2018) as $\nu_t = c_\mu k^2 / \epsilon$, where $c_\mu = 0.09$, k is the turbulent kinetic energy, and ϵ is the dissipation rate.

5.1 Resolvent Analysis

To study the forced dynamics of the bubble, we recast equation (2) into the resolvent form as described in McKeon & Sharma (2010)

$$(-i\omega \mathbf{M} - \mathbf{A}_{2D,z}) \hat{\mathbf{q}} = \mathbf{B} \hat{\mathbf{f}}. \quad (3)$$

The optimal response $\hat{\mathbf{q}} = (\hat{u}, \hat{v}, \hat{w})$ to any harmonic forcing $\hat{\mathbf{f}} = (\hat{f}_x, \hat{f}_y, \hat{f}_z, 0)$ can be obtained by performing a singular value decomposition (SVD) of the resolvent operator \mathbf{R}

$$\hat{\mathbf{q}} = \mathbf{C} (-i\omega \mathbf{M} - \mathbf{A}_{2D,z})^{-1} \mathbf{B} \hat{\mathbf{f}} = \mathbf{R} \hat{\mathbf{f}}, \quad (4)$$

where \mathbf{M} acts as a mass-like matrix, $\mathbf{A}_{2D,z}$ is the two-dimensional LNSE operator ($\bar{\mathbf{u}} = (\bar{u}, \bar{v}, 0)$) and the operators \mathbf{B} and \mathbf{C} act as filters that impose restrictions on the forcing (input) and response (output), respectively. The first singular value of the SVD of the resolvent operator is denoted as the optimal gain σ_1 , while the remaining singular values (sub-optimal gains) are arranged in decreasing order according to

$\sigma_1 > \sigma_2 > \sigma_3 > \dots > \sigma_n$. The computation of the SVD of equation (4) is performed using the code described in Abreu *et al.* (2021) and Blanco *et al.* (2022).

5.2 Global Linear Stability Analysis

When the forcing term $\hat{\mathbf{f}}_0$ is dropped in equation (2) the asymptotic behavior of the TSB flow can be studied by means of the spanwise periodic eigenvalue problem (EVP)

$$-i\omega\mathbf{M}\hat{\mathbf{q}} = \mathbf{A}_{2D,z}\hat{\mathbf{q}}, \quad (5)$$

where $\beta \in \mathbf{R}$ is the spanwise wavenumber, $\omega \in \mathbf{C}$ are the eigenvalues, and $\hat{\mathbf{q}}$ are the eigenfunctions. The EVP in equation (5) can be analyzed to identify unstable global modes whenever the growth rate $\omega_i > 0$, whereas disturbances decay for $t \rightarrow \infty$ when $\omega_i < 0$. The solution to equation (5) is computed using the code from Abreu *et al.* (2021) and Blanco *et al.* (2022), modified for global linear stability analysis.

6 RESULTS AND DISCUSSION

In this section, the results of the resolvent analysis will be presented. In accordance with section 4 we will direct particular focus towards the low-frequency regime $St \simeq 0.01$ and the identified region of spanwise coherence $\beta \simeq 1$. To classify the results, we will further discuss our findings in light of the unsteady experimental database as well as the global linear stability analysis.

6.1 Resolvent Analysis

In figure 5 we depict the optimal energy gain σ_1^2 for different Strouhal numbers St , where we distinguish between the two-dimensional case ($\beta = 0$) and the three-dimensional case ($\beta = 1$). For 2D perturbations ($\beta = 0$), we obtain a distribution that monotonically increases up to $St \approx 0.1$, after which the optimal energy gain rapidly decreases again. In Cura *et al.* (2023) the medium-frequency unsteadiness of the present TSB flow was related to the existence of convective instabilities in the flow. Here, the optimal response at $St = 0.1$ and $\beta = 0$ strongly resembles the typical alternating pattern of Kelvin-Helmholtz (KH) rollers (not shown here), confirming this conclusion. In the case of 3D perturbations ($\beta = 1$), we observe a distinctly different behavior. The highest energy gains are now located in the previously established region of low-frequency unsteadiness $St \simeq 0.01$. Moreover, the optimal energy gain σ_1^2 follows the distribution of a first-order low pass filter with a cut-off frequency $St_c = 0.016$. This value is in good agreement with the values reported for the low-frequency unsteadiness based on pre-multiplied PSDs of fluctuating velocity or wall pressure (e.g., Fig. 3). Notably, the first-order low-pass filter behavior of low-frequency unsteadiness has already been observed experimentally for an incompressible TSB by Mohammed-Taifour & Weiss (2021). It further appears to be a repeated observation in turbulent SBLIs (Plotkin, 1975; Poggie *et al.*, 2015) and has recently been identified in the resolvent analysis of a laminar SBLI (Bugeat *et al.*, 2022).

In figure 6, we display iso-surfaces of the streamwise component of the optimal forcing (left) and response (right) at low frequency $St = 0.01$ and $\beta = 1$. Iso-surfaces of $\pm 45\%$ of $\max|\hat{f}_x|$ and $\max|\hat{u}|$ are shown, respectively. The time-averaged location of the TSB is indicated by the dividing streamline (grey-shaded region). The optimal forcing is located mostly in the region upstream of the separation bubble

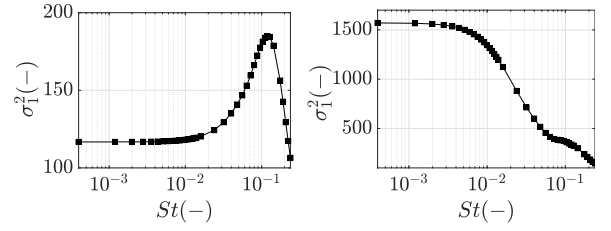


Figure 5. Optimal energy gain σ_1^2 over Strouhal number St for $\beta = 0$ (left) and $\beta = 1$ (right).

and in the first half of the TSB. A spanwise-alternating pattern of large elongated structures, which encompasses a large portion of the domain, becomes evident. The corresponding spanwise wavelength, scaled with the boundary layer thickness δ , is $\lambda_z \approx 20\delta$ at $x/L_p = 0$. The associated optimal response bounds the recirculation region and follows its shape. Interestingly, a similar large-scale “global” structure has been reported for the POD of the streamwise velocity component of the TSB of Mohammed-Taifour & Weiss (2016) and for the SPOD of several pressure-induced TSB flows (Steinfurth *et al.*, 2022; Richardson *et al.*, 2023). In all of these works, the “global” mode was linked with the low-frequency unsteadiness of the TSB. However, the aforementioned works primarily studied the (spectral) POD of the fluctuating velocities in the two-dimensional streamwise/wall-normal plane. Consequently, the three-dimensional structure of the modes was not investigated. Here, the particular spatial configuration of optimal forcing and response, with the forcing mainly located in the upstream region of the TSB and the response restricted to the region nearest to the bubble, suggests that upstream perturbations are a main contribution to the low-frequency unsteadiness. Moreover, resolvent analysis predicts broadly similar behavior in the region $0.25 \leq \beta \leq 3$ and $0.001 \leq \beta \leq 0.01$ (not shown here). That is, similar contours of optimal forcing and response could be observed at low-frequency ($St \simeq 0.01$) and for $0.25 \leq \beta \leq 3$. Furthermore, the abovementioned low-pass filter behavior could be observed for any β within that range. This suggests that the low-frequency unsteadiness most likely is not driven by a unique frequency St and spanwise wavenumber β , but rather, by a range of low frequencies $St \simeq 0.01$ and low, non-zero, spanwise wavenumbers.

In the following we will discuss these results in light of the unsteady experimental database and the global linear stability analysis.

6.2 Discussion

In section 6.1, we have identified a low-frequency resolvent mode with a “global” characteristic and recognized its resemblance to the leading POD/SPOD modes observed in various experimentally measured pressure-induced TSBs. In Towne *et al.* (2018) a direct relationship between the optimal response of RA and the leading SPOD mode was uncovered, when the forcing can be modeled as spatial white noise. Although non-linearities in the Navier-Stokes equations are expected to have “color”, a strong link between these modes can be expected if the resolvent operator is of low-rank (Cavaliere *et al.*, 2019). For the present TSB flow $\sigma_1^2/\sigma_2^2 > 10$ at low frequency, thereby confirming the validity of the low-rank assumption.

Here, we use the SPOD algorithm proposed by Towne *et al.* (2018) on the TR-PIV data of Le Floc’h *et al.* (2020), where $f_s = 900$ Hz, $N_{FFT} = 512$ and a hamming-type window with

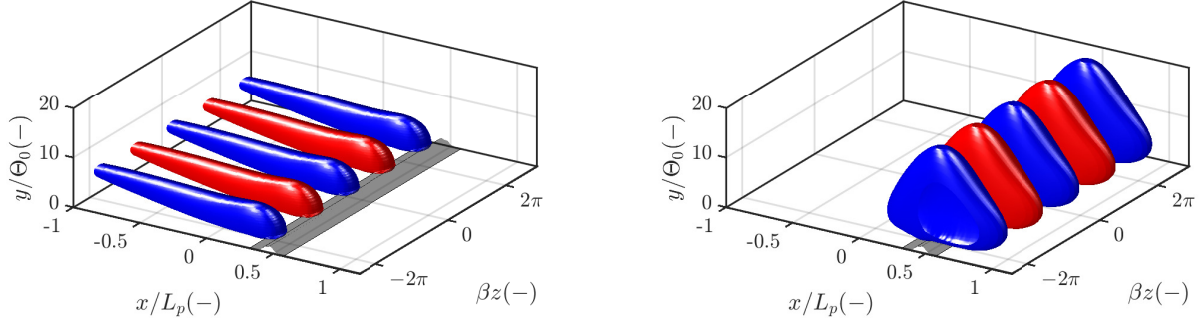


Figure 6. Streamwise component of optimal forcing \hat{f}_x (left) and response \hat{u} (right) for non-dimensional spanwise wavenumber $\beta = 1$. Iso-surfaces of $\pm 45\%$ of the real part of $\max|\hat{f}_x|$ and $\max|\hat{u}|$ are displayed, respectively. The time-averaged location of the TSB is indicated by the dividing streamline (grey-shaded region).

50% overlap was employed. At low frequency $St = 0.01$ the leading SPOD mode represents 72% of the total turbulent kinetic energy (TKE) in the flow, indicating the existence of a dominant flow feature (not shown here). To quantify the alignment between the SPOD and RA modes, we introduce the alignment metric

$$\varphi = \frac{\langle \hat{q}_{1\text{SPOD}}, \hat{q}_{1\text{RA}} \rangle}{\|\hat{q}_{1\text{SPOD}}\| \cdot \|\hat{q}_{1\text{RA}}\|}, \quad (6)$$

which is the projection of the first SPOD mode $q_{1\text{SPOD}}$ on the first RA mode $q_{1\text{RA}}$. Here, $\langle \cdot, \cdot \rangle$ is the L_2 inner product and $\|\cdot\|$ is the euclidean norm. The value $\varphi = 1$ corresponds to perfect alignment of the modes, while $\varphi = 0$ indicates that the modes are orthogonal. Note that only the streamwise and wall-normal component are considered here.

In figure 7 we display the leading SPOD mode (left) and the optimal response from RA (right) at low frequency $St = 0.01$ and $\beta = 1$. The streamwise (top) and wall-normal (bottom) component are displayed, respectively. Clearly, a portion of the large-scale “global” structure described in section 6.1 can be uncovered in the streamwise component of the SPOD of the experimentally measured TSB flow (Fig. 7 left). Similarly, the

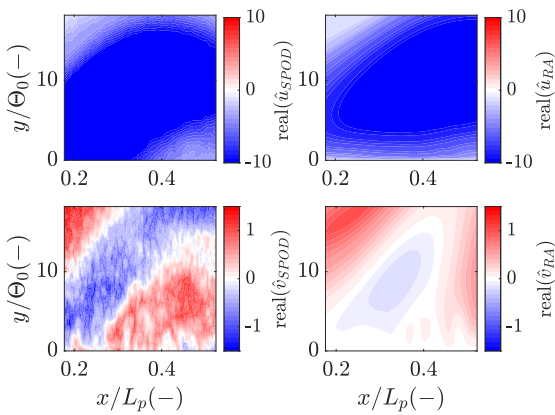


Figure 7. Comparison between leading SPOD mode (left) and optimal response of the RA (right) in the PIV measurement region. The streamwise (top) and wall-normal (bottom) component are depicted, respectively. Results are shown at low-frequency $St = 0.01$ and $\beta = 1$ (RA).

wall-normal component of the leading SPOD mode and the optimal response from RA are in good agreement in terms of phase and position of structures. The alignment is $\varphi = 0.94$. This large value of φ strongly suggests that the low-frequency breathing observed experimentally is associated with the calculated RA response.

Finally, in figure 8 we plot the least stable mode of the GLSA (left) against the optimal response of the RA (right) for $\beta = 1$ and $St = 0.01$ (RA). Interestingly, no growth rate $\omega_i > 0$ could be uncovered for the investigated spanwise wavenumbers β , indicating that the flow is globally stable in the asymptotic time limit. Nevertheless, the striking resemblance between the least stable mode of the GLSA and the optimal response of the RA suggests that the low-frequency receptivity observed in the RA is most likely caused by a modal mechanism driven by this weakly damped global mode. As this low-frequency receptivity has been previously related to the experimentally observed low-frequency unsteadiness (breathing), we propose that the low-frequency breathing of TSBs may be linked to the excitation of this weakly damped global mode. As previously described, this phenomenon is not linked to a unique frequency and spanwise wavenumber, but rather, to a range of low frequencies and low, non-zero spanwise wavenumbers.

7 CONCLUSION

The aim of this work was to investigate the origin of the low-frequency breathing motion commonly observed in pressure-induced turbulent separation bubbles (TSBs). For this purpose, we performed modal and non-modal stability analyses of the numerical DNS base flow from Coleman *et al.* (2018) and compared the results to the unsteady experimental database of Le Floc’h *et al.* (2018, 2020) in a similar flow field. Resolvent analysis revealed strong receptivity to external disturbances at low frequency $St \simeq 0.01$ and low, non-zero spanwise wavenumbers $\beta \simeq 1$. The optimal response was found to closely align with the experimentally measured low-frequency unsteadiness, revealing an alignment of $\varphi = 0.94$ between the leading SPOD mode and the optimal response of RA for $\beta = 1$. The strong similarities between the leading GLSA mode and the optimal response of RA indicate that the low-frequency receptivity might be caused by a modal mechanism, driven by this weakly damped global mode.

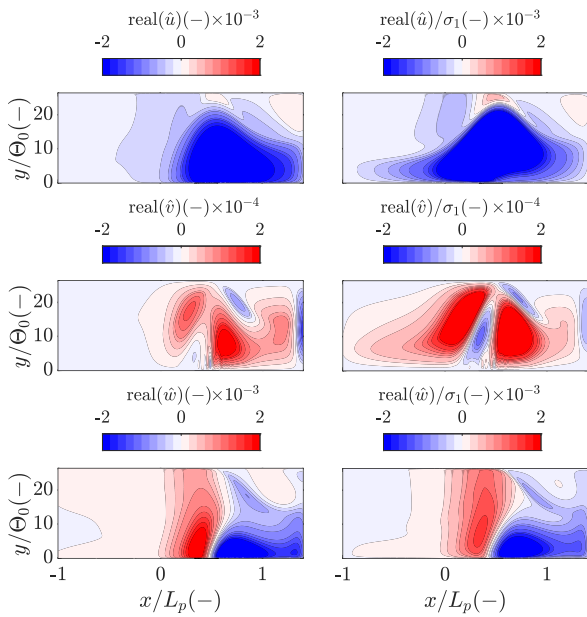


Figure 8. Global LSA mode 1 (left) and optimal response from RA (right) for $\beta = 1$. The streamwise (top), wall-normal (center) and spanwise (bottom) modes are depicted, respectively.

REFERENCES

- Abe, H. 2017 Reynolds-number dependence of wall-pressure fluctuations in a pressure-induced turbulent separation bubble. *Journal of Fluid Mechanics* **833**, 563–598.
- Abreu, L. I., Tanarro, A., Cavalieri, A. V. G., Schlatter, P., Vinuesa, R., Hanifi, A. & Henningson, D. S. 2021 Spanwise-coherent hydrodynamic waves around flat plates and airfoils. *Journal of Fluid Mechanics* **927**, A1.
- Blanco, D. C. P., Martini, E., Sasaki, K. & Cavalieri, A. V. G. 2022 Improved convergence of the spectral proper orthogonal decomposition through time shifting. *Journal of Fluid Mechanics* **950**, A9.
- Bugeat, B., Robinet, J.-Ch., Chassaing, J.-C. & Sagaut, P. 2022 Low-frequency resolvent analysis of the laminar oblique shock wave/boundary layer interaction. *Journal of Fluid Mechanics* **942**, A43.
- Cavalieri, A. V. G., Jordan, P. & Lesshafft, L. 2019 Wavepacket models for jet dynamics and sound radiation. *Applied Mechanics Reviews* **71** (2), 020802.
- Cherry, N. J., Hillier, R. & Latour, M. E. M. P. 1984 Unsteady measurements in a separated and reattaching flow. *Journal of Fluid Mechanics* **144**, 13–46.
- Clemens, N. T. & Narayanaswamy, V. 2014 Low-frequency unsteadiness of shock wave/turbulent boundary layer interactions. *Annual Review of Fluid Mechanics* **46**, 469–492.
- Coleman, G. N., Rumsey, C. L. & Spalart, P. R. 2018 Numerical study of turbulent separation bubbles with varying pressure gradient and Reynolds number. *Journal of Fluid Mechanics* **847**, 28–70.
- Cura, C., Hanifi, A. & Weiss, J. 2023 Medium-frequency unsteadiness in a turbulent separation bubble. In *AIAA SCITECH 2023 Forum*, p. 0095.
- Dolling, D. S. 2001 Fifty years of shock-wave/boundary-layer interaction research: what next? *AIAA Journal* **39** (8), 1517–1531.
- Kiya, M. & Sasaki, K. 1983 Structure of a turbulent separation bubble. *Journal of Fluid Mechanics* **137**, 83–113.
- Le Floc'h, A., Weiss, J., Mohammed-Taifour, A. & Dufresne, L. 2020 Measurements of pressure and velocity fluctuations in a family of turbulent separation bubbles. *Journal of Fluid Mechanics* **902**.
- Le Floc'h, A. S., Mohammed-Taifour, A. T., Dufresne, L. & Weiss, J. 2018 Spanwise aspects of unsteadiness in a pressure-induced turbulent separation bubble. In *2018 Fluid Dynamics Conference*, p. 3538.
- McKeon, B. J. & Sharma, A. S. 2010 A critical-layer framework for turbulent pipe flow. *Journal of Fluid Mechanics* **658**, 336–382.
- Mohammed-Taifour, A. & Weiss, J. 2016 Unsteadiness in a large turbulent separation bubble. *Journal of Fluid Mechanics* **799**, 383–412.
- Mohammed-Taifour, A. & Weiss, J. 2021 Periodic forcing of a large turbulent separation bubble. *Journal of Fluid Mechanics* **915**, A24.
- Na, Y. & Moin, P. 1998 Direct numerical simulation of a separated turbulent boundary layer. *Journal of Fluid Mechanics* **374**, 379–405.
- Plotkin, K. J. 1975 Shock wave oscillation driven by turbulent boundary-layer fluctuations. *AIAA Journal* **13** (8), 1036–1040.
- Poggie, J., Bisek, N. J., Kimmel, R. L. & Stanfield, S. A. 2015 Spectral characteristics of separation shock unsteadiness. *AIAA Journal* **53** (1), 200–214.
- Reynolds, W. C. & Hussain, A. K. M. F. 1972 The mechanics of an organized wave in turbulent shear flow. part 3. theoretical models and comparisons with experiments. *Journal of Fluid Mechanics* **54** (2), 263–288.
- Richardson, R., Zhang, Y., Cattafesta, L. N. & Wu, W. 2023 Low frequency characteristics of a pressure-gradient induced turbulent separation bubble. In *AIAA SCITECH 2023 Forum*, p. 0079.
- Steinfurth, B., Cura, C. & Weiss, J. 2022 Three-dimensional effects associated with the low-frequency breathing motion of a turbulent separation bubble. In *20th International Symposium on Application of Laser and Imaging Techniques to Fluid Mechanics, Lisbon*.
- Towne, A., Schmidt, O. T. & Colonius, T. 2018 Spectral proper orthogonal decomposition and its relationship to dynamic mode decomposition and resolvent analysis. *Journal of Fluid Mechanics* **847**, 821–867.
- Weiss, J., Mohammed-Taifour, A. & Schwaab, Q. 2015 Unsteady behavior of a pressure-induced turbulent separation bubble. *AIAA Journal* **53** (9), 2634–2645.
- Wu, W., Meneveau, C. & Mittal, R. 2020 Spatio-temporal dynamics of turbulent separation bubbles. *Journal of Fluid Mechanics* **883**.